Supersonic Axisymmetric Flow over Boattails Containing a Centered Propulsive Jet

George S. Deiwert*
NASA Ames Research Center, Moffett Field, California

The influence of underexpanded jets on a supersonic afterbody flowfield is investigated using computational techniques. The thin-shear-layer formulation of the compressible, Reynolds-averaged, Navier-Stokes equations is solved using a time-dependent, implicit numerical algorithm. Solutions are obtained for supersonic flow over an axisymmetric conical afterbody containing a centered propulsive jet where the freestream Mach number is 2.0 and the jet exit Mach number is 2.5. Exhaust-jet static pressures are considered in the range of 2 to 9 times the freestream static pressure and with nozzle-exit half-angles from 15 to 43 deg. Comparisons are made with experimental results for base pressure, separation distance, afterbody pressure distribution, and flowfield structure. Although good quantitative agreement with experimental separation distance and base pressure level is not observed, the parametric trends induced by exhaust-jet pressure level and nozzle-exit angle are well predicted, as well as the flowfield details in the vicinity of the afterbody and in the exhaust plume.

Introduction

THE aerodynamic drag associated with afterbody configurations is influenced both by the afterbody geometry and the interaction of the exhaust with the external flow. For propulsive units such as jet engines and rocket motors, the exhaust plumes are highly underexpanded and their influence on base pressure and flow over the afterbody can be large, inducing in some instances extensive regions of flow separation. The flowfield for these configurations is complex, exhibiting regions of strong viscous/inviscid interaction, strong viscous/viscous interaction, and regions of flow recirculation. For engineering design calculations extensive use is made of component modeling methods that provide quick estimates of base pressure and base region slipstreams. For a more comprehensive description of the flowfield details and a straightforward prediction of afterbody flow separation in regions of strong interaction, full field approaches that describe the interactions in a fully coupled manner, while considerably more expensive to use, are necessary at this time.

Previous studies of related flows using the full field approach include the works of: 1) Mikhail et al.,[1] in which the supersonic flow over a boattailed afterbody with a jet-exit Mach number of one and a jet-to-freestream pressure ratio of 3.75 is simulated on a 39 × 30 grid; 2) Peery and Forester,[2] in which transonic flow over a multistream supersonic nozzle is simulated on a 2765 point grid; 3) Waskiewicz et al.,[3] in which the supersonic near wake of a backward facing step is simulated on a 64 × 45 grid; 4) Sullins et al.,[4] in which the supersonic near wake over a backward facing step with parallel injection is simulated using a 50 × 20 grid; 5) Hasen,[5] in which the supersonic flow in the base region of a supersonic axisymmetric nozzle is simulated on a 45 × 45 grid for overexpanded jets and on a 57 × 45 grid for slightly underexpanded jets; and 6) Mace et al.,[6] in which supersonic flow in the base region of a supersonic axisymmetric nozzle operating at a jet-to-freestream pressure ratio of 1.5 is simulated with combustion effects on a 21 × 17 grid. In all of the above examples except the last, the explicit MacCormack method is used to solve the Reynolds-averaged Navier-Stokes equations numerically, while in the last example the parabolized Navier-Stokes equations are solved using a marching scheme and the species concentrations determined using a Newton-Raphson iteration procedure. In each of the examples, the discretized computational space is too coarse to resolve the high gradient regions in the shear layers and, hence, are not suitable for the prediction of skin friction or separation. Peery and Forester recognized this and used wall functions to describe the near wall shear layer for attached flows. More recently, Sahu et al.[7] studied the flowfield in the base region of a cylindrical body for transonic flow and, using an implicit method to solve the thin-layer approximation to the Reynolds-averaged, Navier-Stokes equations and a 108 × 50 grid, resolved the wall shear layer to the scale of the viscous-dominated sublayer.

This paper describes a computational investigation of the influence of exhaust pressure and nozzle-exit angle on the character of the afterbody flowfield. The time-dependent, Reynolds-averaged compressible Navier-Stokes equations are solved numerically using the thin-layer approximation for supersonic flow over an axisymmetric conical afterbody containing a centered propulsive jet. The freestream Mach number is 2.0, the jet-exit Mach number is 2.5, the jet-exit pressure is varied from 2 to 9 times the freestream pressure, and conical nozzle half-angles up to 43 deg are considered. Both the external flow and the exhaust are ideal air at a common total temperature. The Reynolds number of the external flow based on forebody diameter is 1.5×10^6. The computations correspond, in part, to a series of experiments by Agrell and White[8] for the same configuration and flow conditions.

Configuration

The geometric configuration is a nine-caliber body of revolution comprised of a 14-deg half-angle conical nose, a cylindrical forebody, and an 8 deg half-angle conical afterbody of one-caliber length. Centered inside the afterbody is a conical nozzle with an exit diameter of 0.6 caliber that is flush with the afterbody base. The conical nozzle half-angle is varied parametrically from 15 to 43 deg.

Governing Equations

Following the procedure described by Nietubicz et al.[9] the axisymmetric, two-dimensional, time-dependent, Reynolds-averaged, Navier-Stokes equations for compressible flow are

---

Presented as Paper 83-0462 at the AIAA 21st Aerospace Sciences Meeting, Reno, Nev., Jan. 10-13, 1983; submitted Feb. 4, 1983; revision submitted Dec. 23, 1983.

*Research Scientist. Member AIAA.

written in general curvilinear coordinates in strong conservative form with the approximation that shear layers are thin and aligned with one principal plane:

$$\partial_\tau q + \partial_\xi E + \partial_\eta F + H = Re^{-1} \partial_\eta S \qquad (1)$$

where general coordinate transformations

$$\xi = \xi(x,y,t), \quad \eta = \eta(x,y,t), \quad \tau = t$$

are used, and

$$q = J^{-1} \begin{bmatrix} \rho \\ \rho u \\ \rho v \\ e \end{bmatrix}, \quad E = J^{-1} \begin{bmatrix} \rho U \\ \rho u U + \xi_x p \\ \rho v U + \xi_y p \\ (e+p) U - \xi_t p \end{bmatrix}$$

$$F = J^{-1} \begin{bmatrix} \rho V \\ \rho u V + \eta_x p \\ \rho v V + \eta_y p \\ (e+p) V - \eta_t p \end{bmatrix}, \quad H = J^{-1} \begin{bmatrix} 0 \\ 0 \\ p/\eta \\ 0 \end{bmatrix}$$

$$S = J^{-1} \begin{bmatrix} 0 \\ \mu(\eta_x^2 + \eta_y^2) u_\eta + (\mu/3)(\eta_x u_\eta + \eta_y v_\eta)\eta_x \\ \mu(\eta_x^2 + \eta_y^2) v_\eta + (\mu/3)(\eta_x u_\eta + \eta_y v_\eta)\eta_y \\ ((\eta_x^2 + \eta_y^2)[0.5\mu(u^2+v^2)_\eta + \mu(a^2)_\eta/(\gamma-1)Pr] \\ + (\mu/3)(\eta_x u + \eta_y v)(\eta_x u_\eta + \eta_y v_\eta)) \end{bmatrix}$$

The ξ coordinate is body oriented in the streamwise direction and the η coordinate is radial, normal to the body surface and downstream cylindrical axis. The velocities $U = \xi_t + \xi_x u + \xi_y v$ and $V = \eta_t + \eta_x u + \eta_y v$ represent the contravariant velocity components in the ξ and η directions, respectively.

The Cartesian velocity components (u,v) are retained as the dependent variables and are nondimensionalized with respect to the freestream speed of sound, a. Nondimensional pressure is defined as

$$p = (\gamma - 1)[e - 0.5(u^2 + v^2)]$$

where γ is the ratio of specific heats, density ρ is referenced to ρ_∞, and the total energy e is referenced to $\rho_\infty a_\infty^2$. The additional parameters are κ, the coefficient of thermal conductivity; μ, the dynamic viscosity; Re, the Reynolds number based on body diameter; and Pr, the Prandtl number.

The metric terms of Eq. (1) are defined from

$$\xi_x = J\eta y_\eta, \quad \xi_y = -J\eta x_\eta, \quad \xi_t = J\eta(x_\eta y_\tau - x_\tau y_\eta)$$

$$\eta_x = -J\eta y_\xi, \quad \eta_y = J\eta x_\xi, \quad \eta_t = -J\eta(x_\tau y_\xi + y_\tau x_\xi)$$

$$J^{-1} = \eta(x_\xi y_\eta - x_\eta y_\xi)$$

The "thin-layer" approximation used here requires that critical body surfaces be mapped onto $\eta = \text{const}$ planes, and that $Re \gg 1$. The variation of the viscous terms in the coordinate direction along the body surface (here taken as ξ) is neglected, and terms in the η or near-normal direction to the body surface are retained.

To solve Eq. (1), the Beam and Warming[10] implicit finite difference algorithm is used. Written in operator notation, and using approximate factorization to facilitate efficient use of vector processors, the difference equation is

$$\mathcal{L}_\xi \mathcal{L}_\eta \Delta_t q = \mathcal{R}_\xi + \mathcal{R}_\eta - \Delta\tau H^n$$

where

$$\mathcal{L}_\xi = (I + h\delta_\xi A^n - \epsilon_I J^{-1} \nabla_\xi \Delta_\xi J)$$

$$\mathcal{L}_\eta = (I + h\delta_\eta B^n - \epsilon_I J^{-1} \nabla_\eta \Delta_\eta J - hRe^{-1} \delta_\eta J^{-1} M^n J)$$

$$\Delta_t q = q^{n+1} - q^{n-1}$$

$$\mathcal{R}_\xi = -\Delta\tau \delta_\xi E^n - \epsilon_E J^{-1} (\nabla_\xi \Delta_\xi)^2 J q^n$$

$$\mathcal{R}_\eta = -\Delta\tau(\delta_\eta F^n - Re^{-1} \delta_\eta S^n) - \epsilon_E J^{-1} (\nabla_\eta \Delta_\eta)^2 J q^n$$

where the δ_ξ and δ_η are central difference operators, ∇_ξ and ∇_η and Δ_ξ and Δ_η are backward- are forward-difference operators in the ξ and η directions, respectively. For example, $\Delta_\eta q = q(\xi, \eta + \Delta\eta) - q(\xi, \eta)$. Indices denoting spatial location have been suppressed for convenience. The Jacobian matrices $A = \partial_q E$ and $B = \partial_q F$, along with the coefficient matrix M, obtained from the local time linearization of S, are described in detail in Ref. 11. Fourth-order explicit (ϵ_E) and second-order implicit (ϵ_I) terms have been added to control nonlinear instabilities.

An implicit method was chosen to avoid restrictive stability conditions which occur when small grid spacing is used. Highly refined grids are needed to obtain spatial accuracy and resolution of large gradients which occur when calculating viscous effects. Small grid sizes may also occur because nonoptimal mappings overly concentrate points in some regions. Implicit methods are useful in avoiding stiffness in problems in which the solution is forced. In such cases, time steps that are large compared to those demanded by an explicit stability limit often can be taken without degradation of accuracy.

The basic algorithm is first- or second-order accurate in time and noniterative. The equations are factored (spatially split), which reduces the solution process to two one-dimensional problems at a given time level. Central difference operators are employed, and the algorithm produces block-tridiagonal systems for each space coordinate. The stability and accuracy of the numerical algorithm are described by Warming and Beam.[12] Linear analysis of the numerical scheme shows that it is unconditionally stable, although in actual practice the nonlinear equations are subject to a time-step limitation. The limitation, though, is usually less stringent than what is found for conventional explicit schemes. For the steady-state cases presented herein first-order time accuracy is used with second-order accuracy in space.

Computational Grid

A body-oriented computational grid is constructed in a manner compatible with the thin-layer approximation. Shown in Fig. 1 is the grid used in the computations in the present investigation; Fig. 1a shows the complete configuration in physical space, Fig. 1b shows the detail in the base region of the afterbody, and Fig. 1c shows the computational space domain. Radial grid lines on the forebody join the surface orthogonally. On the afterbody and in the exhaust plume the radial lines are normal to the body axis. There are 89 points distributed along the body, with appropriate clustering, of which 22 are on the afterbody. Another 48 points are distributed downstream of the afterbody to a distance equal to 10 forebody diameters from the nozzle base. Points are distributed radially from the body surface to a distance equal to 20 forebody diameters both ahead of and normal to the body. A total of 48 points is used in this region, with a high degree of stretching used in order to resolve the sublayer of the turbulent boundary layer. An additional 32 points are distributed across the nozzle and its blunt base from the centerline to the afterbody surface. One- and two-parameter hyperbolic-tangent stretching functions are used in the base region to focus resolution near the corners and achieve a smooth, piecewise continuous distribution of points across the exhaust plume and base. At the nozzle exit, points are distributed along an arc describing the conical-flow exit plane (that is, the arc radius is equal to the nozzle-exit radius divided by the sine of the nozzle-exit half-angle). Downstream of the nozzle, the grid lines are aligned to closely approximate the exhaust plume shape as suggested by experimentally obtained schlieren photographs by Agrell and White[8] for a 20-deg half-angle conical nozzle with a jet pressure nine times that of the freestream. The total computational grid of 137 × 80 is used to generate a solution from an impulsive start for flow with an exhaust jet having a pressure equal to twice the freestream pressure. This grid construction remains fixed during the course of the solution development, but it is recognized that adaptive meshing, particularly near and just downstream of the afterbody, would be more desirable in order to better define the plume boundary and resolve regions with large gradients.

Wall-dominated viscous effects in the base region will not be supported by the grid used in the present study. One reason for this is that the viscous terms are not carried in the shear-layer equations [Eq. (1)], and another is that the computational grid does not have sufficient resolution to capture the very small wall-dominated length scales. Both of these reasons can be overcome by including thin-layer terms in the ξ direction, and increasing the resolution of the grid near the base region. Neither of these steps is necessary for the goals of the present effort since wall-turbulence effects in the base-flow region are expected to be small compared with other flowfield features. This approximation is consistent with previous studies described in Refs. 1 and 3-7.

Initial and Boundary Conditions

For supersonic external flow it is computationally expedient to impose supersonic inflow conditions just ahead of the afterbody and not to carry the forebody through the computation process. Ideally, forebody solutions could be determined using more efficient methods (e.g., parabolized methods), and used as upstream boundary conditions for the afterbody computation. However, unless very good guesses for the starting flowfield are used, particularly when there are high-pressure exhaust jets, strong transient disturbances from the base region will propagate forward through the boundary layer and destroy the validity of the solution, or even cause the numerical scheme to fail to converge. Hence, in the present studies, the flow over the entire configuration is computed as a whole for the first solution using the lower-valued jet-to-freestream pressure ratio of 2. In this case, the body is impulsively started with conical exhaust-jet conditions imposed at the jet-exit plane. This converged solution constitutes a very good guess for the next case to be computed that has the same external flow conditions; it is used as the starting solution. In all subsequent cases, the first seven calibers of the configuration are disregarded, and supersonic inflow conditions are imposed as determined from solution for the entire configuration. The computational grid in these computations is 82 × 80 and ignores the grid in the first seven calibers of the forebody.

Other boundary conditions consist of 1) no-slip, adiabatic wall and zero normal pressure gradient on the forebody and afterbody surface, 2) uniform freestream at the far-field lateral boundary, 3) extrapolation at the downstream boundary, 4) inviscid conical flow at the jet-exit plane, 5) slip and impermeable adiabatic wall with zero normal pressure gradient at the nozzle base, and 6) symmetry at the jet centerline with zero radial density gradient. When the entire flowfield is computed from an impulsive start, the upstream boundary condition is a uniform freestream, and symmetry conditions are imposed on the upstream centerline emanating from the conical nose.

To approximately account for viscous mixing at the interface of the inviscid jet at the exit plane and the viscous flow in the base region, a 20% mixing, with conservation preserved, is imposed at the two points just downstream of the nozzle lip that straddle the exhaust-jet/base-flow boundary. In addition, at the corners of the base the boundary conditions are double-valued and depend on the direction from which the corner is approached. When approaching the external corner from the radial direction, the no-slip condition is used with zero normal pressure gradient determined from the radial direction; when approaching both corners from the streamwise direction the slip boundary condition is used with a zero normal pressure gradient determined from the streamwise direction.

Turbulence Model

Turbulence transport is described here using eddy-viscosity concepts, and empirical models are used to determine the coefficients (μ_T) that are combined with the molecular transport viscosity coefficients to describe the total shear. To simplify the analysis in the present study, algebraic eddy-viscosity models are used and at present no attempt is made to account for strong compressibility effects in the exhaust plume, nor to account for flow-history effects on viscosity, either through convective transport or relaxation concepts. Rather, local scalar descriptions are used that imply local equilibrium. Clearly there are flow regimes where these assumptions are not strictly valid (such as flow where there is strong viscous/inviscid interaction and in the interaction of a high-pressure exhaust jet with the external flow). The relaxation of these assumptions and the study of more realistic or complex turbulence models is left for future study.

Dimensional analysis dictates that eddy-transport coefficients μ_T are proportional to a length scale l times a velocity scale v. In simple wall-shear flows, the length scale very close to the wall is simply the distance away from the wall, and the length scale for the outer part of the layer is proportional to a boundary-layer thickness parameter. The velocity scales in these regions are generally expressed in terms of the well-defined length scale times the local velocity gradient across the shear layer ($\mu_T \; \alpha \; l^2 \partial v / \partial \eta$). For fully developed jets and wakes, the length scale is determined by the jet or wake width, and the velocity scale is determined by the difference in velocity from the centerline to the edge. For more complex shear flows, these scales (particularly the length scale) are not as well defined.

The algebraic eddy-viscosity model used in this study is due to Baldwin and Lomax.[13] This model is particularly well suited to complex flows that contain regions in which the length scales are not clearly defined. It is described briefly as follows: For wall-bounded shear layers a two-layer formulation is used such that

$$\begin{aligned} \mu_T &= (\mu_T)_{\text{inner}} \qquad && \eta < \eta_{\text{crossover}} \\ &= (\mu_T)_{\text{outer}} \qquad && \eta > \eta_{\text{crossover}} \end{aligned}$$

where η is the normal distance from the wall and $\eta_{\text{crossover}}$ is the smallest value of η at which values from the inner and outer formulas are equal. The Prandtl-Van Driest formulation is used in the inner (or wall) region,

$$(\mu_T)_{\text{inner}} = \rho l^2 \, |\omega|$$

where

$$l = \kappa \eta \, [1 - \exp(-\eta^+ / A^+)]$$

$$\eta^+ = (\rho_w \tau_w)^{1/2} \eta / \mu_w, \quad \kappa = 0.4, \quad A^+ = 26$$

and $|\omega|$ is the magnitude of the local vorticity,

$$|\omega| = |\partial_y u - \partial_x v|$$

The formulation for the outer region is given by

$$(\mu_T)_{\text{outer}} = 0.0168 C_{cp} F_{\text{wake}} F_{\text{Kleb}}(\eta)$$

$$F_{\text{wake}} = \begin{pmatrix} \eta_{\max} F_{\max} \\ C_{wk} \eta_{\max} U^2_{\text{dif}} / F_{\max} \end{pmatrix} \text{ the smaller}$$

$$C_{cp} = 1.6, \quad C_{wk} = 0.25, \quad C_{\text{Kleb}} = 0.3$$

The quantities $\eta_{\max}$ and $F_{\max}$ are determined from the function

$$F(\eta) = \eta\, |\omega|\, [1 - \exp(-\eta^+ / A^+)]$$

where $F_{\max}$ is the maximum value of $F(\eta)$, and $\eta_{\max}$ is the value of η at which it occurs. The function $F_{\text{Kleb}}(\eta)$ is the Klebanoff intermittency function given by

$$F_{\text{Kleb}}(\eta) = (1 + 5.5 (C_{\text{Kleb}} \eta / \eta_{\max})^6]^{-1}$$

The quantity U_{dif} is the difference between the maximum and minimum total velocity in the profile (along a coordinate line),

$$U^2_{\text{dif}} = (u^2 + v^2)_{\max} - (u^2 + v^2)_{\min}$$

and for boundary layers the minimum is defined as zero.

The advantages of this model for boundary layer flows are as follows: 1) for the inner region, the velocity and length scales are always well defined, and the model is consistent with the "law of the wall"; 2) in the outer region, for well-behaved (simple) boundary layers, where there is a well-defined length scale ($\eta_{\max}$), the velocity scale is determined by $F_{\max}$, which is a length scale times a vorticity scale; 3) in the outer region of complex boundary layers where the length from a wall becomes meaningless, a new length scale is determined from a velocity (U_{dif}) divided by a velocity gradient ($|\omega|$), and the velocity scale is U_{dif}.

The outer formulation that is independent of η is also used in the free-shear flow regions (exhaust plume and wake), as well as over regions of separated flow and regions of strong viscous/inviscid interaction. In these regimes, the Van Driest damping term $[\exp(-\eta^+/A^+)]$ is neglected. For jets and wakes, the Klebanoff intermittency factor is determined measuring from the centerline, and the minimum term in U_{dif} is evaluated from the profile rather than being defined as zero.

The validity of the eddy-viscosity model constants for high-pressure exhaust jets has not been established, and it is re-emphasized that compressibility effects are not accounted for.

At the exhaust-jet exit plane and in the near-base region, the eddy viscosity is assumed to be negligibly small and grows to the value given by the outer model over a short distance downstream of the base. For the present results, a linear streamwise relaxation procedure was used between the jet-exit plane and the ninth plane downstream of the jet-exit plane to define the eddy viscosity between the jet centerline and the outer edge of the shear layer. To approximate the effect of the conical nozzle boundary layer on jet mixing at the nozzle exit, a two-point conservative mixing is imposed at the nozzle lip, as described earlier in the section on boundary conditions.

Results

Solutions were obtained for exhaust-jet-to-freestream pressure ratios of 2, 3, 5, 7, and 9. Shown in Fig. 2 are computed density contours and streamlines for a pressure ratio of 3 and a nozzle-exit half-angle of 20 deg. Superposed for comparison are key flow features—traced from the schlieren photograph published by Agrell and White[8] for the same geometry and flow conditions—which show the following features. First, at the forebody/afterbody junction there is an expansion wave emanating from the junction at an angle of 36 deg to the freestream. This is accompanied by a turning of the streamlines to follow the contour of the 8-deg half-angle afterbody surface. Second, at the end of the afterbody there is an oblique compression shock at an angle of 33 deg to the freestream, accompanied by a turning of the

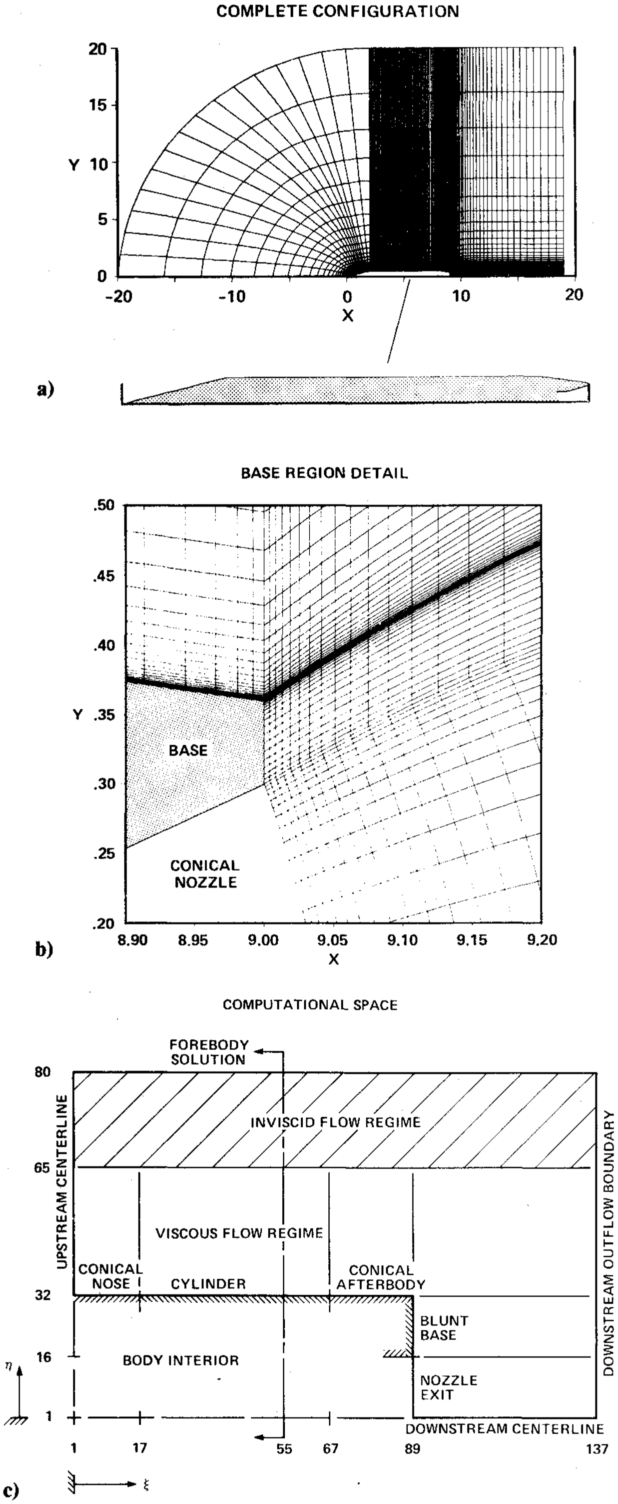

Fig. 1 Computational grid for FFA boattail with propulsive jet: a) complete grid detail, physical space; b) nozzle-base region detail; c) complete region in computational space.

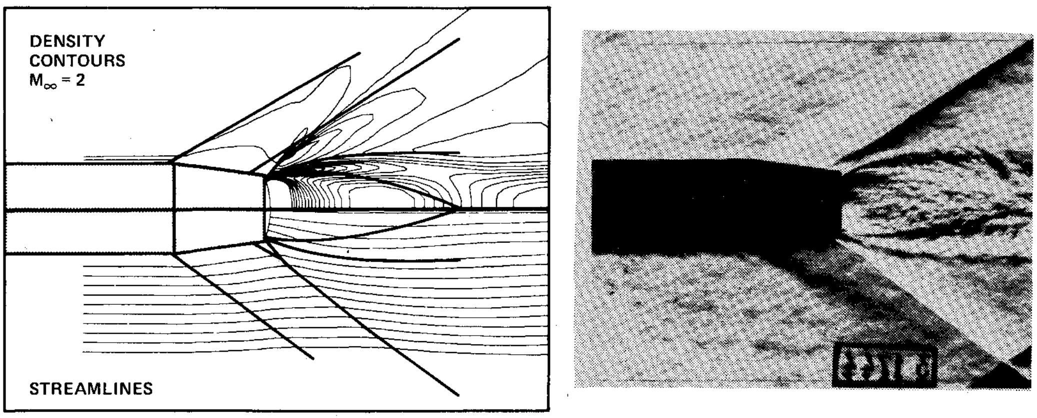

Fig. 2 Computed density contours (top) and streamlines (bottom) for 8-deg conical afterbody with 20-deg nozzle; experimental features from schlieren photograph superposed: $P_j/P_\infty = 3$, $M_\infty = 2$, $M_j = 2.5$.

streamlines to follow the exhaust plume. Third, near the corner, the shock bifurcates to a lambda shock with the upstream leg impinging the boundary layer of the afterbody. Fourth, a slipline emanates from the nozzle lip and defines the exhaust plume/external flow boundary. Finally, inside the plume there is a barrel shock that closes just over two calibers downstream of the exit plane. The agreement between computed and experimentally observed flow features is excellent in nearly every respect. A difference in the shape of the barrel shock near the closure at the centerline of the exhaust plume is caused by imposition of a density gradient of zero across the centerline on the coarse grid used in the numerical simulation. It would be computationally more precise to use a finer radial grid resolution in this region and to impose a second-order extrapolation on the density boundary condition to enforce symmetry.

Figure 3 shows the computed flowfield details in the base region for the same conditions as those in Fig. 2. Velocity vectors and streamlines are shown in Fig. 3a. The boundary layer on the afterbody exhibits a very small separation bubble which is induced by the upstream leg of the lambda shock just ahead of the aft end of the afterbody. Near the outer edge of the blunt base is a trapped vortex of clockwise recirculating flow. The fluid from the boundary layer over the afterbody surface swirls around this trapped vortex back toward the nozzle base where, as it approaches the lip, it is entrained by the exhaust plume. In Fig. 3b, Mach contours show a subsonic region extending downstream of the base as defined by the region inside the contour line for $M = 1.0$. At the nozzle lip there is a strong Prandtl-Meyer expansion from the high-pressure exhaust jet to the low-pressure base region.

As the exhaust-jet exit pressure is increased, the details of the flow features change. Figure 4 shows computed density contours and streamlines for a jet-to-freestream pressure ratio of 9 and a nozzle exit half-angle of 25 deg. Superposed for comparison are key flow features traced from a schlieren photograph published by Agrell and White[8] for the same flow conditions but for a nozzle half-angle of 20 deg. (The experimental study of Agrell and White considered nozzle half-angles only up to 20 deg. The schlieren features used for comparison with the computed results represent data for the experimental flow conditions that most nearly correspond with the computed flow conditions.) Again there is good agreement between the key flowfield features indicated by the computed results an the experimentally observed results. In this higher exhaust pressure flow, the lambda compression shock induces a large separation region on the afterbody. Shown in Fig. 5 are computed flowfield details in the base region for this higher jet pressure case.

In Fig. 5a are velocity vectors and streamlines. The boundary layer on the afterbody shows the extensive separation bubble that is outlined by a dividing streamline. In contrast to the solution shown for the lower jet pressure in Fig. 3, there is no trapped vortex on the nozzle base indicated in Fig. 5a. The recirculation region is confined to the boundary layer on the afterbody around which the fluid is turned and pulled around the nozzle base where, as it ap-

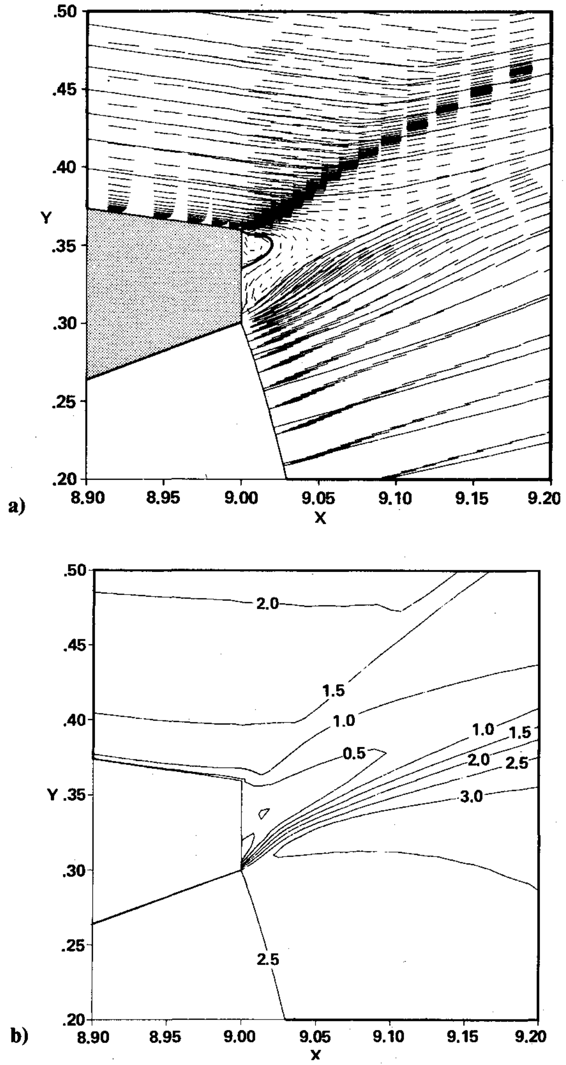

Fig. 3 Base region detail for 8-deg conical afterbody with 20-deg nozzle: $P_j/P_\infty = 3$, $M_\infty = 2$, $M_j = 2.5$. a) Velocity vectors and streamlines; b) Mach contours.

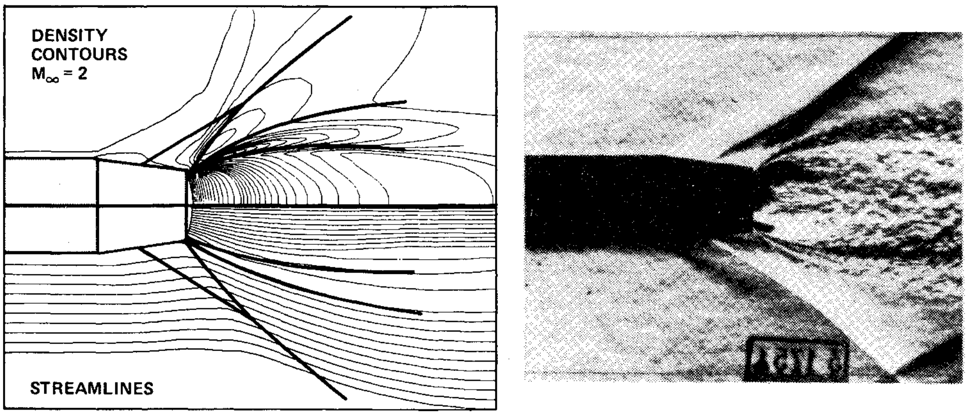

Fig. 4 Computed density contours (top) and streamlines (bottom) for 8-deg conical afterbody with 25-deg nozzle; experimental features from schlieren photograph for 20-deg nozzle superposed: $P_j/P_\infty = 9$, $M_\infty = 2$, $M_j = 2.5$.

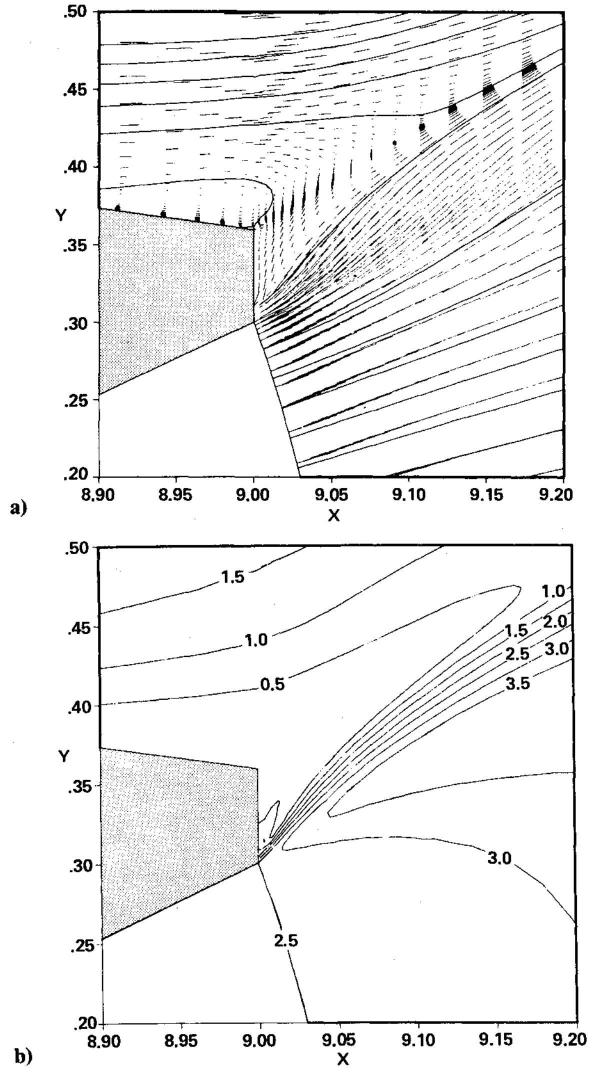

Fig. 5 Base region detail for 8-deg conical afterbody with 25-deg nozzle: $P_j/P_\infty = 9$, $M_\infty = 2$, $M_j = 2.5$. a) Velocity vectors and streamlines; b) Mach contours.

proaches the nozzle lip, it is entrained by the exhaust plume. The higher pressure exhaust jet has displaced the external compression shock to a position more forward on the afterbody compared with the lower pressure jet. The Mach contours shown in Fig. 5b indicate a large subsonic region extending from far above the afterbody surface to far downstream of the nozzle base.

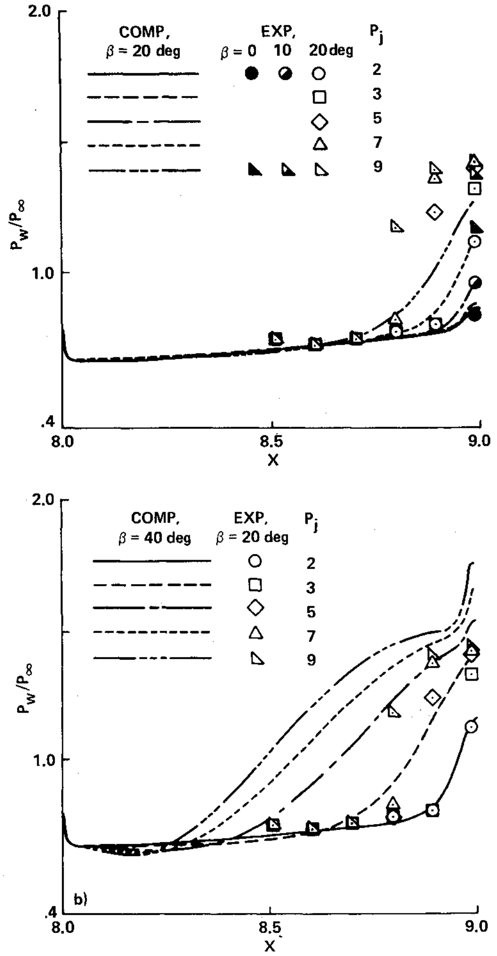

Fig. 6 Afterbody surface-pressure distribution: $M_\infty = 2$, $M_j = 2.5$. a) 20-deg nozzle-exit angle; b) 40-deg nozzle-exit angle.

The influence of jet pressure on the afterbody surface-pressure distribution is shown in Figs. 6a and 6b, where surface pressure over the afterbody is shown as a function of axial position on the afterbody for jet-pressure ratios of 2, 3, 5, 7, and 9. The underexpanded exhaust jet induces a pressure rise over the aft portion of the afterbody, the level and extent of which increase with jet-to-freestream pressure ratio. This effect is much greater for larger nozzle-exit angles, as can be seen by comparing the solutions for the 40-deg nozzle in Fig. 6b with the solutions for the 20-deg nozzle in Fig. 6a. Included for comparison are some experimental data from Agrell and White. These data show the same trend of afterbody pressure

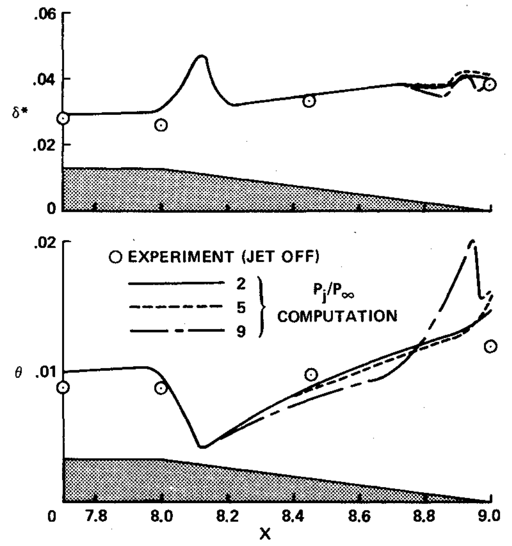

Fig. 7 Boundary-layer parameters over afterbody with 20-deg nozzle: $M_\infty = 2$, $M_j = 2.5$. Displacement thickness and momentum thickness.

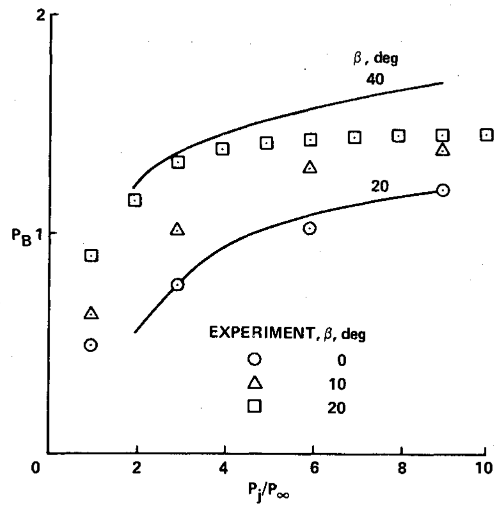

Fig. 8 Nozzle-base pressure variation with jet-to-freestream pressure ratio: $M_\infty = 2$, $M_j = 2.5$.

distribution as influenced by jet-pressure ratio and nozzle-exit angle, but differ in quantitative detail, particularly by indicating similar levels and trends for smaller nozzle-exit angles. Specific explanations for the quantitative differences between computed and experimental pressure distributions are not yet clear, especially in view of the relatively good agreement observed in the flowfield features indicated by the schlieren photographs and computed density contours and streamlines. Quantitative differences are likely to be associated with the details of the jet expansion around the nozzle lip and with the details of the viscous/inviscid interaction and associated boundary-layer separation on the afterbody surface. There is fairly coarse resolution in the computational grid in the nozzle lip region where there exists a very strong expansion to the low-pressure base region. Also, the viscous/viscous interaction model used in the computation in this region is ad hoc and is not totally adequate, and no attempt was made to describe the nozzle boundary layer or any upstream influence that may propagate through this boundary layer. And, for conical nozzles with exit half-angles of 20 deg and greater, the assumption of conical flow at the nozzle-exit plane is not really compatible with what is observed experimentally where it is known that the jet begins to depart from a truly conical flow. In the external flow where the viscous/inviscid interaction is large, there is some considerable uncertainty in the validity of the turbulence model that is based on local equilibrium conditions for incompressible flows. The susceptibility of the boundary layer to separation is certainly influenced by the turbulence transport model used. Nevertheless, the parametric trends, showing the influence of jet pressure ratio and nozzle exit angle, are predicted and compare with experimentally observed trends.

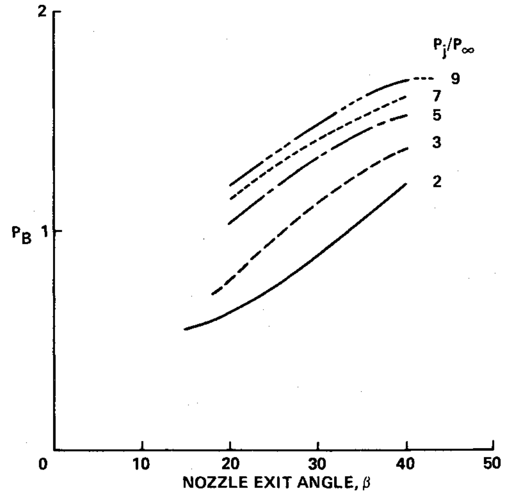

Fig. 9 Nozzle-base pressure variation with nozzle-exit angle: $M_\infty = 2$, $M_j = 2.5$.

The influence of jet pressure on the afterbody boundary layer is shown in Figs. 7a and 7b where displacement thickness δ^* and momentum thickness θ distributions over the afterbody are shown for pressure ratios of 2, 5, and 9 for the 20-deg conical nozzle. Figure 7a shows the displacement thickness which exhibits an increase in magnitude just aft of the forebody/afterbody junction followed by a recovery back to the undisturbed level. At the end of the afterbody, where there is a viscous/inviscid interaction, there are mild excursions in the displacement thickness distribution that increase somewhat with increased jet pressures. Included for comparison are experimentally measured displacement thicknesses by Agrell and White for a jet-off case (pressure ratio of zero). Figure 7b shows momentum thickness that exhibits a rapid decrease just aft of the forebody/afterbody junction followed by a gradual increase to the end of the afterbody. For a pressure ratio of 9 there is a rapid increase in momentum thickness over the last 20% of the afterbody, the region where there is a strong viscous/inviscid interaction.

The influence of jet-exit pressure on nozzle-base pressure is seen in Fig. 8, which shows a monotonic increase in base pressure with jet pressure and an increase with nozzle-exit angle. Included also are experimental data of Agrell and White which show the same parametric variation, but differ in quantitative level for reasons suggested previously. A leveling off of base pressure with increased values of jet pressure for higher nozzle-exit angles, as suggested by experimental data, is not observed in the computed results. The parametric influence of nozzle-exit angle on base pressure is more clearly illustrated in Fig. 9, which shows base pressure increasing monotonically with exit angle for five different exhaust pressure ratios.

The influence of jet pressure on afterbody separation is shown in Fig. 10 where s, the axial separation length measured upstream from the end of the afterbody, is plotted as a function of jet-pressure ratio for both the 20- and 40-deg nozzle computations. Separation distance increases with both jet-pressure ratio and nozzle-exit angle. The 20-deg nozzle results show very little separation for the lower jet pressures,

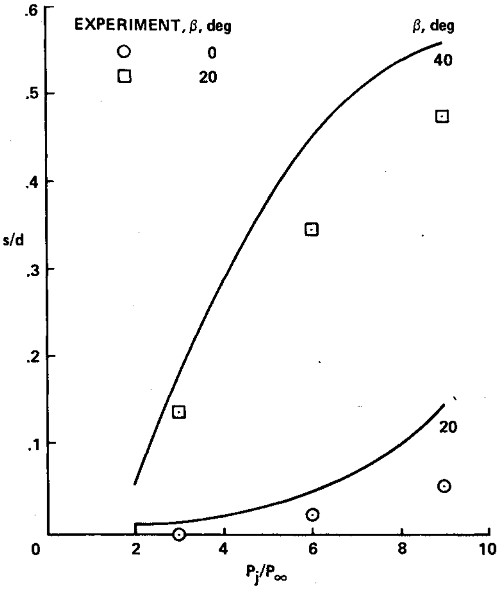

Fig. 10 Afterbody separation length variation with jet-to-freestream pressure ratio: $M_\infty = 2$, $M_j = 2.5$.

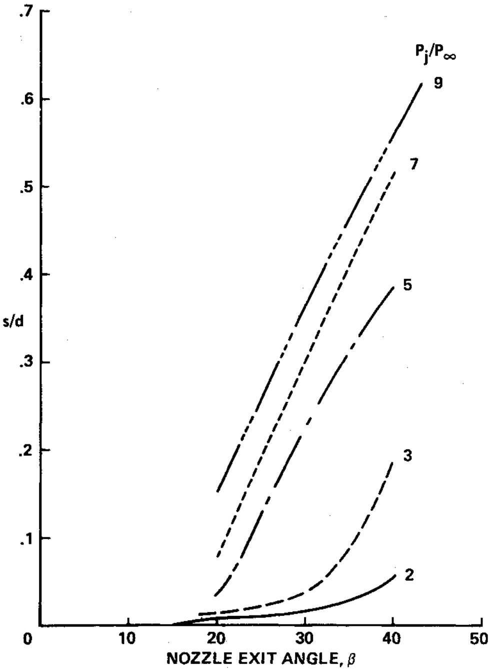

Fig. 11 Afterbody separation length variation with nozzle-exit angle. $M_\infty = 2$, $M_j = 2.5$.

but the separation length increases at an increasing rate as the jet pressure is further increased. The 40-deg nozzle results show a rapid increase in separation length with jet pressure until the separation distance is about half the afterbody length; this distance increases less rapidly with further increase in jet pressure. Parametric trends indicated by experimental data of Agrell and White are similar although the nozzle-exit angles differ. The parametric effect of nozzle-exit angle on afterbody separation length is shown in Fig. 11 for the five different jet-pressure ratios considered. A monotonic increase of separation length with exit angle is indicated.

Concluding Remarks

The influence of underexpanded jets on a supersonic afterbody flowfield has been investigated computationally. The thin-shear-layer approximation of the compressible, Reynolds-averaged, Navier-Stokes equations was solved numerically to simulate a Mach-2 external flow over a conical afterbody containing a Mach-2.5 centered propulsive jet. Jet-to-freestream ratios of 2, 3, 5, 7, and 9 and conical nozzle-exit half-angles from 15 to 43 deg were considered. Comparisons with experimental data of Agrell and White for the same configuration and flow conditions indicate that many key flow features, such as exhaust plume shape and structure and external compression shocks, are well predicted, and that parametric trends, such as the influence of exhaust pressure and nozzle-exit angle on the variation of nozzle-base pressure and afterbody separation scales, are described well. Typically, however, trends with respect to nozzle-exit angle occurred in the experimental study by Agrell and White for smaller angles than were indicated in the present study. The absence of good quantitative comparison with respect to nozzle-exit angle suggests that further study is needed, with attention focused essentially on the details of the expansion region at the nozzle lip and on the turbulent transport model in the vicinity of viscous/inviscid interaction and associated boundary-layer separation.

References

[1] Mikhail, A. G., Hankey, W. L., and Shang, J. S., "Computation of a Supersonic Flow Past an Axisymmetric Nozzle Boattail with Jet Exhaust," *AIAA Journal*, Vol. 18, Aug. 1980, pp. 869-875.

[2] Peery, K. M. and Forester, C. K., "Numerical Simulation of Multistream Nozzle Flows," AIAA Paper 79-1549, 1979.

[3] Waskiewicz, J. D., Shang, J. S., and Hankey, W. L., "Numerical Simulation of Near Wakes Utilizing a Relaxation Turbulence Model," *AIAA Journal*, Vol. 18, Dec. 1980, pp. 1440-1445.

[4] Sullins, G. A., Anderson, J. D., Jr., and Drummond, J. P., "Numerical Investigation of Supersonic Base Flow with Parallel Injection," AIAA Paper 82-1001, 1982.

[5] Hasen, G. A., "Navier-Stokes Solutions for an Axisymmetric Nozzle," *AIAA Journal*, Vol. 20, Sept. 1982, pp. 1219-1227.

[6] Mace, A.C.H., Markatos, N. C., Spalding, D. B., and Tatchell, D. G., "Analysis of Combustion in Recirculating Flow for Rocket Exhausts in Supersonic Streams," *Journal of Spacecraft and Rockets*, Vol. 19, Nov.-Dec. 1982, pp. 557-563.

[7] Sahu, J., Nietubicz, C. J., and Steger, J. L., "Numerical Computation of a Base Flow for a Projectile at Transonic Speeds," AIAA Paper 82-1358, Aug. 1982.

[8] Agrell, J. and White, R. A., "An Experimental Investigation of Supersonic Axisymmetric Flow over Boattails Containing a Centered Propulsive Jet," The Aeronautical Research Institute of Sweden, Stockholm, Tech. Note AU-913, 1974.

[9] Nietubicz, C. J., Pulliam, T. H., and Steger, J. L., "Numerical Solution of the Azimuthal-Invariant Thin-Layer Navier-Stokes Equations," AIAA Paper 79-0010, Jan. 1979.

[10] Beam, R. and Warming, R. F., "An Implicit Finite-Difference Algorithm for Hypersonic Systems in Conservation-Law-Form," *Journal of Computational Physics*, Vol. 22, Sept. 1976, pp. 87-110.

[11] Pulliam, T. H. and Steger, J. L., "Implicit Finite-Difference Simulations of Three-Dimensional Compressible Flow," *AIAA Journal*, Vol. 18, Feb. 1980, pp. 159-169.

[12] Warming, R. F. and Beam, R., "On the Construction and Application of Implicit Factored Schemes for Conservation Laws," *SIAM-AMS Proceedings of the Symposium on Computational Fluid Mechanics*, Vol. 11, New York, 1977, pp. 85-129.

[13] Baldwin, B. S. and Lomax, H., "Thin Layer Approximation and Algebraic Model for Separated Turbulent Flows," AIAA Paper 78-257, 1978.